Asian Journal of Pharmaceutical Sciences 16 (2021) 794–805

Available online at www.sciencedirect.com

ScienceDirect

journal homepage: www.elsevier.com/locate/AJPS

Original Research Paper

Multifunctional self-delivery micelles targeting the invasion-metastasis cascade for enhanced chemotherapy against melanoma and the lung metastasis

Shanshan Xu[a,1], *Chunyu Liu*[b,1], *Shuya Zang*[a], *Jiaxin Li*[a], *Yashi Wang*[a], *Kebai Ren*[a], *Man Li*[a], *Zhirong Zhang*[a], *Qin He*[a,*]

[a] *West China School of Pharmacy, Sichuan University, Chengdu 610041, China*
[b] *Pharmacy Department, West China Hospital, Chengdu 610041, China*

ARTICLE INFO

Article history:
Received 18 January 2021
Revised 2 August 2021
Accepted 19 August 2021
Available online 16 September 2021

Keywords:
Self-delivery system
Chondroitin sulfate
Tumor metastasis
Multiphase

ABSTRACT

Metastasis is closely related to the high mortality of cancer patients, which is regulated by multiple signaling pathways. Hence, multiphase blocking of this biological process is beneficial for cancer treatments. Herein, we establish a multifunctional self-delivering system by synthesizing D-α-tocopheryl succinates (TOS)-conjugated chondroitin sulfate (CS) (CT NPs), which both serve as nanocarrier and antimetastatic agent that affects different phases of the metastatic cascade. TOS as the hydrophobic segment of CT NPs can inhibit the secretion of matrix metalloproteinase-9, while the hydrophilic segment CS targets B16F10 cells through CD44 receptors and reduces the interaction between tumor cells and platelets. The results show that CT NPs are able to inhibit metastasis successfully both *in vitro* and *in vivo* by interfering the multiphase of the metastatic cascade. Following encapsulating chemotherapeutic drug doxorubicin (DOX), the obtained micelles CT/DOX efficiently suppress both primary-tumor growth and metastases in B16F10 bearing mice. As a result, the rationally designed multifunctional NPs composing of biocompatible materials provide excellent therapeutic effects on solid tumors and metastases.

1. Introduction

Metastasis is responsible for the overwhelming cause of cancer-associated mortality [1–3], therefore, metastasis suppression is the key to reducing cancer mortality and improving therapeutic effect [4,5], while the conventional therapeutic strategies are ineffective when dealing with small clusters of invasive malignant cells [6,7], and the inhibitors against metastasis cascade may be inadequate for treating large, solid tumor *in situ*. Such situation highlights the significance of constructing a multifunctional drug delivery system, which can both remove primary tumors and inhibit tumor metastasis to new organs.

* Corresponding author.
E-mail address: qinhe@scu.edu.cn (Q. He).
[1] The authors contributed equally.
Peer review under responsibility of Shenyang Pharmaceutical University.

https://doi.org/10.1016/j.ajps.2021.08.002

Tumor metastasis is an extremely complicated, multistep biological process known as the invasion-metastasis cascade [8,9]. It mainly includes cancer cell motility, intravasation, survival in the circulation, extravasation, establishment of microenvironment and eventually formation of micrometastasis [2,10,11]. From a therapeutic standpoint, understanding the pathways and steps that lead to successful metastasis will help us design rational therapeutic strategies and construct feasible delivery systems. So far, potential therapeutic strategies and functional delivery nanosystems have been used to inhibit metastasis by targeting vital molecules and relevant signaling pathways [12]. Various therapeutic interventions are reported, including protease inhibitors that prevent the degradation of extracellular matrix (ECM), integrin antagonists to inhibit the adhesion between tumor cells and platelets, and cell membrane-cloaking drug delivery nanosystem for capturing and clearing circulating tumor cells (CTCs) etc. [10,13,14]. Nevertheless, due to the multifactorial and intricate cascade process, inhibition of single phase may not be sufficient to eliminate the metastasis [15,16]. Therefore, targeting the multiphase molecules and biological processes involved in invasion-metastasis cascade may improve the treatment of invasive cancers.

All organs and tissues consist of cells and non-cellular components, which form the ECMs. ECMs serve as the physical scaffolds into which cells are embedded. At the same time, it will influence many cellular processes, such as metastasis and invasion of tumors [17–19]. Matrix metalloproteinase 9 (MMP-9) expressed in many tumor cells can degrade the ECMs and remodel the microenvironment [20–23], which is beneficial for the detachment and invasion of tumor cells [24]. D-α-tocopheryl succinate (TOS), an analogue of vitamin E, is able to increase the apoptosis of various types of tumor cells [25–27]. Our previous study has found that TOS can significantly reduce the secretion of MMP-9 in various tumor cells [28], including B16F10 melanoma cells. As a result, TOS is able to prevent the degradation of ECMs through interfering MMP-9, and thus reduce the shedding of tumor cells from the primary site. Meanwhile, hematogenous metastasis and lymphatic metastasis are two main pathways of tumor metastasis, among which platelets play an important role [14,29]. Growing body of experimental evidence has demonstrated that platelets are favorable to metastasis [30,31]. Platelets can form a “coat” on the tumor through the adhesion between tumor cells and platelets, which protects the tumors cells from flow shear stress and immune elimination, thus helping the CTCs survive in the circulation and assist CTCs cross the endothelium [32,33]. Cluster determinant 44 (CD44) is overexpressed on various tumor cells [34–36]. Hyaluronic acid (HA) and chondroitin sulfate (CS) are natural substrates that can specifically interact with CD44, and will be beneficial for tumor targeting [28,37]. Research has shown that CS derivatives show a better affinity with CD44 than HA derivatives with the same molecular weight and degree of substitution [38]. As a part of the ECMs, CS, a linear polysaccharide, possessed the advantages of biodegradability, biocompatibility, and low immunogenicity [39]. Besides, chondroitin sulfate glycosaminoglycans (CS-GAGs) on cancer cells can serve as P-selectin ligands, and exogenous CS can reduce the adhesion between tumor cells and platelets by hindering P-selectin which is expressed on activated platelets. Consequently, CS can prevent CTCs from implanting at distant organs [40–43].

The rapid development of drug delivery nanosystems has brought new opportunities for the treatment of solid tumors and their metastasis. Compared with small-molecule chemotherapeutic drugs, nano-carriers can improve the distribution of drugs *in vivo* and mainly deliver drugs to specific tissues such as brain, liver, lung and lymph nodes [44]. In order to enhance the anticancer effect, self-delivery nanosystems such as the prodrug strategy have been widely applied [45]. Inspired by this, we constructed a self-delivery micelle with CS and TOS (CT) (Fig. 1), of which the hydrophilic and hydrophobic segments possess anti-metastasis effect. The multifunctional micelle serves as the nano-carriers of chemotherapeutic drugs for enhanced tumor targeting; in the meantime, it also acts as antimetastatic agents that affect different phases of the metastatic cascade.

Here, we developed a simple self-delivery micelle CT, and the drug doxorubicin (DOX) was packaged in the hydrophobic core. The micelle was designed for suppressing tumor growth and metastasis in B16F10 bearing mice. As a typical chemotherapeutic drug, DOX has serious side effects, especially cardiotoxicity, while CT NPs can enhance the accumulation of DOX in tumor sites to reduce side effects. After accumulation in tumor tissues, CT/DOX NPs were internalized via endocytosis, releasing DOX in the acidic intracellular environment to kill tumor cells effectively. In this present study, we investigated the characterizations, cytotoxicity, anti-migration effect and *in vivo* therapeutic efficacy of CT/DOX NPs. Besides, the *in vivo* antimetastasis effects and the attenuation of toxicity of DOX by CT NPs were also evaluated.

2. Materials and methods

2.1. Materials

Chondroitin sulfate (CS) was purchased from Aladdin (Shanghai, China). D-a-tocopheryl succinate (TOS) and Doxorubicin hydrochloride (DOX•HCl) (>98%) were purchased from Melonepharma (Dalian, China). 1-(3-Dimethylaminopropyl)−3-ethylcarbodiimide Hydrochloride (EDCI) (>99%), N–Hydroxy-succinimide (NHS) (>98%), 4-(Dimethylamino) pyridine (DMAP) (>99%) and Pyrene (98%) were purchased from J&K Scientific (Beijing, China). Cell activity and cell proliferation detection kit (CCK-8) was obtained from APE x BIO (USA). BD Matrigel TM Basement Membrane Matrix was obtained from BD Biosciences (San Jose, CA, USA). Calcein-AM, 1,1′-dioctadecy1–3,3,3′3’-tetra-methylindodicarbocyanine(DiD),6-diamidino-2-phenylindole (DAPI) were obtained from Beyotime Biotechnology (Shanghai, China) Annexin V-FITC / PI apoptosis kit were obtained from KeyGEN BioTECH (Jiangsu, China). Carboxyfluorescein succinimidyl amino ester (CFSE) was obtained from Dojindo (Kumamoto, Japan). Rabbit anti-CD44 antibody, Rabbit anti-MMP9 antibody and goat anti-rabbit IgG (H + L) HRP were obtained from Abways Technology (USA). Plastic cell culture dishes and plates were obtained from

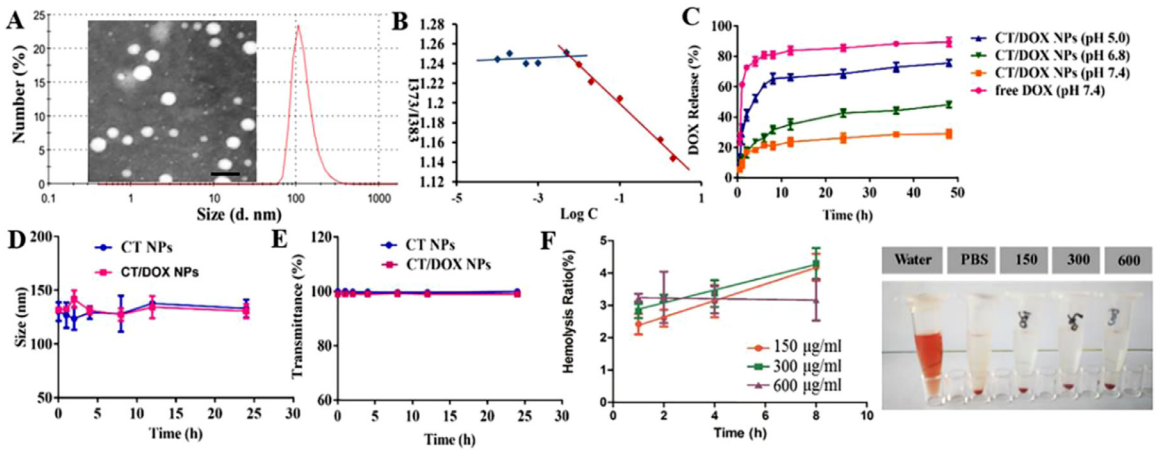

Fig. 1 – (A) Transmission electron microscopy (TEM) image and dynamic light scattering (DLS) size distribution of CT/DOX NPs. (B) The CMC of the CT NPs. (C) Cumulative amount of DOX released from free DOX, CT/DOX NPs in different conditions at 37 °C within 48 h. (means ± SD, $n = 3$). (D) Stability of NPs represented by size and E) transmittance when incubated in 50% FBS for 24 h at 37 °C. (means ± SD, $n = 3$). (F) Hemolysis ratio and images of red blood cells treated with CT/DOX NPs at various concentrations (means ± SD, $n = 3$).

Wuxi NEST Biotechnology Co. (Wuxi, China). All chemicals and reagents were used without further purification.

Mouse melanoma cells (B16F10) and mouse embryonic fibroblast cells (NIH 3T3) were obtained from the Shanghai Institutes for Biological Sciences, CAS (SIBS, Shanghai, China). All cells were cultured in RPMI-1640 medium (GIBCO) supplemented with 10% FBS (HyClone), 100 μg/ml streptomycin and 100 U/ml penicillin at 37 °C, 5% CO_2 atmosphere. C57BL/6 mice (male, 6–8 week, 20 ± 2 g, and specific pathogen free) were purchased from Dossy Experimental Animals Co., Ltd. (Chengdu, China). All animal experiments were performed on the basis of the principles of Experimental Animals Administrative Committee of Sichuan University.

2.2. *Synthesis of CS-TOS conjugates*

CT conjugates were obtained by connecting TOS to CS via ester linkage. In brief, TOS (1.5 mmol), EDCI (3 mmol), NHS (3 mmol) and DMAP (0.7 mmol) were added to DMF (12 ml), and the mixture were stirred at 30 °C for 3 h to activate the carboxyl group of TOS. CS (1 mmol) in formamide (6 ml) were added slowly into activated TOS solution. The reaction was conducted at 30 °C for 48 h under constant stirring. After that, the solution was precipitated via ice-cold acetone to remove the excessive TOS. The precipitate was dissolved in purified water and then dialyzed exhaustively with dialysis membrane (MWCO:3500) to remove the catalysts and solvent, finally products were lyophilized. The structure of conjugate was characterized by ^{1}HNMR spectroscopy and IR spectroscopy. The content of CS in CT conjugate was determined by phloroglucinol method [46].

2.3. *Preparation and characterization of CT/DOX NPs*

DOX•HCl (10 mg), trimethylamine (15 μl) was dissolved in ethanol (5 ml) and stirred overnight in the dark. Ethanol was removed by rotary evaporation and dichloromethane (DCM, 5 mL), ethanol (1 ml) were added to dissolve DOX. The DOX solution was directly mixed with CT conjugate (100 mg) at room temperature for 3 h with constant stirring. Then, purified water (50 ml) was dropped into the mixture and followed by ultrasonication (100 W, 5 s/5 s, 10 min). The organic solvent was removed by rotary evaporation, subsequently, the red emulsion was dialyzed with dialysis membrane (MWCO:3500) against purified water for 6 h. Finally, the retentate was lyophilized after filtering through the filter (0.22 μm).

CT/DOX NPs and blank micelles were reconstituted in aqueous buffers. The particle size, zeta potential and PDI were characterized using Malvern Zetasizer Nano-ZS90 (Malvern Instruments Ltd., U.K). With the help of the transmission electron microscope, we observed the morphology of NPs (Hitachi H-600, Japan). Drug loading efficiency and Entrapment efficiency of NPs were measured by fluorescence photometer at Ex = 505 nm and Em = 594 nm.

$$\text{Loading efficiency}(\%) = (\text{quality of DOX in micelles})/(\text{quality of DOX} - \text{loaded NPs}) \times 100\%,$$

$$\text{Entrapment efficiency}(\%) = (\text{quality of DOX in micelles})/(\text{quality of total DOX}) \times 100\%.$$

2.4. *In vitro stability of CT/DOX NPs*

The variations of particle size and transmittance were investigated to evaluate the stability of NPs. Briefly, CT and CT/DOX NPs were mixed with equal volume of PBS and FBS, respectively, and incubated at 37 °C, 75 r/min. At each pre-set point, the particle size of NPs was measured by Dynamic relight scattering (DLS). Meanwhile, 200 μl of samples were drawn into a 96-well plate to measure the absorbance at 750 nm by Multiskan Spectrum (Thermo Scientific Varioskan Flash).

2.5. Hemolysis test

The blood compatibility of the NPs was investigated by hemolysis test. Whole blood of C57BL/6 mouse was collected into anticoagulant tubes. After centrifugation, the red blood cells (RBCs) were obtained. For every 20 μl of RBCs, 1 ml PBS buffer with pH 7.4 was added to obtain a concentration of 2% RBCs suspension. CT NPs (1200 μg/ml, 600 μg/ml, and 300 μg/ml) were incubated with 2% RBCs, PBS buffer treated RBCs was served as negative control and water treated RBCs was served as positive control. At 1 h, 2 h, 4 h and 8 h, samples were centrifuged at 1500 rpm for 10 min, the supernatant was added to the 96-well plate, and the absorbance of each group was determined at 540 nm with a Multiskan Spectrum and the precipitated erythrocytes were observed under microscope. Hemolysis ratio of each group was calculated according to the following formula.

$$\text{Hemolysis ratio}(\%) = \left(A_{sample} - A_{PBS}\right)/(A_{water} - A_{PBS}) \times 100\%$$

2.6. DOX release from CT/DOX NPs

Release behavior of CT/DOX NPs *in vitro* was performed in PBS buffer at 37 °C, 75 rpm. Briefly, we used ultrapure water to dilute the prepared CT/DOX NPs, and the free DOX of the same concentration was used as the control group, 1 ml CT/DOX NPs and free DOX were loaded into dialysis bags (MWCO = 7 kDa), respectively, and then immersed in PBS buffer (50 ml) at different pH values (pH 7.4, 6.8 and 5.0). At predetermined time point, 400 μl of the release media was collected, meanwhile, 400 μl the fresh medium was added. The amount of released DOX was determined at Ex = 505 nm and Em = 594 nm with a microplate reader.

2.7. Cellular uptake and competitive inhibition assay in vitro

B16F10 and NIH 3T3 cells were seeded in six-well plates at a density of 5×10^5 cells per well. Cells were incubated at 37 °C, 5% CO_2 to obtain 70%–80% cell confluence. Half of the groups were incubated with chondroitin sulfate solutions (2 mg/ml) prior to block the CD44 receptor for 2 h, and then free DOX and CT/DOX NPs (DOX-equivalent 2.5 μg/ml) were added to each well, respectively, and cultured under the same condition for 4 h. After the incubation, cells were rinsed several times by cold PBS (pH 7.4) and suspended in 500 μl of PBS. The mean DOX fluorescence of each group was measured using flow cytometer (Cytomics FC 500, Beckman Coulter, USA).

For qualitative analysis, we used the confocal laser scanning microscopy (CLSM) to investigate the competitive inhibition assay, B16F10 cells were seeded in six-well plates (5×10^5 cells per) with a coverslip placed at the bottom. The culture conditions were the same as previously described. Cells were rinsed with cold PBS (pH 7.4) and fixed with 4% paraformaldehyde. After that, we used 1 μg/ml DAPI solutions to label nucleus for 10 min. Images were gathered by CLSM (LSM 800, Zeiss, Germany).

2.8. In vitro inhibitory effect on cell migration and invasion

Wound healing and invasion assays were performed to evaluate the anti-migration and anti-invasion ability of NPs. For wound healing assay, B16F10 cells were cultured to obtain approximately 95% confluence in six-well plates. Then we used a 200-μl pipette tip to generate a straight line and rinsed with cold PBS (pH 7.4). Subsequently, the cells were incubated with 2% serum medium containing PBS, free DOX, CS, CT NPs, CT/DOX NPs (DOX-equivalent 0.5 μg/ml), for 24 h, respectively. Images of the scratch were collected at 0 and 24 h with an inverted microscope (DMi1, Leica, Germany). The relative scratch-healing percentage was calculated by Image J.

For invasion assays, 50 μl of Matrigel was added into the top chamber of Transwell plate (24-well inserts, 8.0 μm pores). Then the Transwells plate was put into the humidified incubator for 1 h. Cells (1×10^5) were added in the upper chambers, meanwhile, 600 μl of 20% serum-containing medium was added into the lower chamber. After the cells were adhered, 2% serum medium containing free DOX, free CS, CT NPs, CT/DOX NPs (DOX-equivalent 0.5 μg/ml) were added to the upper chamber, respectively and incubated for 48 h. The invaded cells were fixed with 4% (m/V) paraformaldehyde solution and stained by 0.1% crystal violet solution, finally, washed with ultrapure water and imaged. The cells were eluted with 33% acetic acid solution and measured by Multiskan Spectrum at 570 nm.

2.9. In vitro expression of MMP-9

B16F10 cells incubated to obtain 60–70% cell confluence in six-well plates. Afterwards, cells were treated with serum-free medium containing PBS, CS or CT NPs for 30 h. Then, cells were lysed and centrifuged at 4 °C, 12 000 rpm, and the supernatant mixed with loading buffer ($V_{supernatants}/V_{loading\ buffer} = 4{:}1$) was used for Western blot assay. The protein samples were separated by 6% SDS-PAGE and then transferred to a polyvinylidene difluoride membrane (PVDF membranes). The PVDF membrane was incubated with rabbit anti-MMP9 primary antibody at 4 °C for 12 h, then, incubated with HRP-labeled secondary antibody at 37 °C for 2 h. Finally, the bands were measured by Bio-Rad ChemiDoc MP System (Bio-Rad Laboratories, Hercules, USA) and semi-quantitatively measured by Image J.

2.10. Adhesion of platelets to tumor cells in vitro and implantation of B16F10 cells in lung tissues

Platelet-rich plasma was obtained from male C57BL/6 mice, followed by centrifugation and washing with PBS to get platelets. The platelets were labeled with calcein AM for 20 min and re-suspended with PBS [45]. Then, B16F10 cells were incubated to obtain approximately 80% confluence in six-plates. Culture medium was substituted with fresh serum-free medium containing PBS, free CS, DOX, CT NPs or CT/DOX NPs, respectively. After culturing for 30 min, calcein-AM marked platelets were added and incubated for another 30 min. Cells were rinsed with PBS (pH 7.4) and lysed with

1% TritonX-100 solution. Finally, the fluorescence intensity of each group was measured by fluorescence spectrophotometer (RF-6000, Shimadzu, Japan).

C57BL/6 mice were randomly divided into four groups and administrated with PBS, free CS, CT NPs or CT/DOX NPs (DOX-equivalent 3 mg/kg) 30 min in advance. At the same time, B16F10 cells were stained with carboxyfluorescein succinimidyl ester (CFSE) with a concentration of 20 μM (37 °C, 15 min). Then, 1×10^6 CFSE-labeled cells were injected into mice through the tail vein. At 30 min after injection, lungs were harvested. The distribution of B16F10 cells in frozen sections of lungs was collected by CLSM. The fluorescence signal of CFSE was detected at $E_x = 496$ nm and $E_m = 516$ nm.

2.11. Tumor-targeting biodistribution studies

The CT NPs were marked with DiD through physical entrapment. CT conjugates and free DiD were added to DCM and stirred for 3 h. After that, PBS was added into the mixture (pH = 7.4, V_{PBS}:V_{DCM}= 5:1) followed by sonication (100 w, 10 min). DCM was removed by rotary evaporation. Component solvent containing propylene glycol and PBS ($V_{propylene\ glycol}$:V_{PBS} = 1:1) were used to dissolve free DiD.

The B16F10 subcutaneous tumor model was constructed by inoculating 1×10^6 B16F10 cells into the right backs of C57BL/6 mice. Upon the tumor volume grew approximately 500 mm^3, the mice were put into three groups randomly and given with PBS, free DiD or CT/DiD NPs (20 μg DiD per mouse). At 1, 4, 8 and 24 h, the fluorescence in the tumor site of anesthetized mice were analyzed by an *in vivo* imaging system (IVIS, PerkinElmer, USA). Beyond that, mice were euthanized at 24 h, major organs and tumors were harvested and imaged by IVIS. Meanwhile, the distribution of CT NPs in tumors site at 24 h was captured using CLSM.

2.12. In vivo anti-tumor efficacy

The B16F10 subcutaneous tumor model was constructed according to a previously described method. Upon the tumor volume grew about 50 mm^3 (at day 5 after the injection of B16F10 cells), the mice were randomly put into 4 groups ($n = 5$) and treated with PBS, free CS, free DOX or CT/DOX NPs (DOX-equivalent 3 mg/kg). The treatment was given every two days for total five times. The weight of mice and volume of tumor were recorded every 2 d (Tumor volume = $L \times W^2/2$, L means larger diameter and W means smaller diameter). On Day 18, mice were sacrificed, and tumors were harvested and imaged. Meanwhile, hematoxylin and eosin (H&E) staining was conducted for histological analysis of tumor tissues and major organs. The mean tumor growth inhibition rate (%) = $(1 - V_{treatment} / V_{PBS}) \times 100$, in which $V_{treatment}$ and V_{PBS} were the average tumor volumes at Day 18 of the treatment group and PBS group, respectively.

2.13. In vivo anti-metastasis efficacy

Lung metastasis model of B16F10 melanoma was constructed to evaluate the anti-metastatic efficacy of CT/DOX NPs. Briefly, 0.1 ml of PBS containing 1×10^6 B16F10 cells were injected through tail vein. On Day 4, the mice were put into 5 groups ($n = 5$). Subsequently, the mice were administered PBS, free DOX, free CS, CT NPs or CT/DOX NPs (DOX-equivalent 3 mg/kg) every 2 d for total five times. The weight of mice was recorded throughout the treatment period. On Day 24, the mice were sacrificed, lungs were harvested and imaged. Meanwhile, H&E staining was used for histological analysis of lung tissues.

2.14. Preliminary safety evaluation

Healthy C57BL/6 mice were randomly put into 5 groups ($n = 3$) and treated with PBS, free DOX, free CS, CT NPs or CT/DOX NPs via tail vein (DOX-equivalent 3 mg/kg), respectively. The treatment was given every 2 d for total five times. 24 h after the final administration, sangue intero was collected by retro-orbital bleeding. A small amount of blood was taken into the anticoagulative tubes for routine blood test (Mindray, BC-2800Vet, China). The rest of the blood was centrifuged for 15 min at 3000 rpm after standing at 37 °C for 2 h to obtain serum for the biochemical analysis (TECOM, TC6010L, China).

2.15. Statistical analysis

All data were exhibited as the mean ± standard deviations (SD), $n = X$, in which "X" means the sample quantity. For multiple groups, significant differences was determined by one-way ANOVA, Statistical significance was indicated by $^*P < 0.05$, $^{**}P < 0.01$ and $^{***}P < 0.001$.

3. Results and discussion

3.1. Characterization of CT/DOX NPs

CS and TOS were conjugated by esterification reaction to form the CS-TOS (CT) conjugates (Fig. S1). The structures of CT conjugate were confirmed by ^{1}H NMR spectra and IR spectra. In the ^{1}H NMR spectrum (Fig. S2), the characteristic peaks of CS (δ=3.27–4.66) and TOS (δ=0.79–1.86) were clearly observed in CT conjugates (Fig. S2C and S2D). In the IR spectrum, 3305.96 cm^{-1} and 1608.31 cm^{-1} were the characteristic bands of CS (Fig. S3A). Bands at 2924.08 cm^{-1} and 1751.00 cm^{-1} were attributed to the methylene group and carbonyl group in TOS, respectively (Fig. S3B). As for CT conjugates (Fig. S3C), the methylene peak of TOS (2925.57 cm^{-1}) was observed, as well as the carbonyl peak of the ester bond at 1643.73 cm^{-1}. All of these observations verified the formation of ester bond between hydroxyl group of CS and carboxyl group of TOS.

Particle size of CT/DOX NPs was 137.87 ± 2.32 nm with narrow distribution (PDI = 0.12 ± 0.01) and the zeta potential was −26.73 ± 0.97 mV (Tab. S1). CT/DOX NPs exhibited uniform and spherical appearance under a transmission electron microscope (TEM) observation, and the particle size was about 100 nm in the TEM images (Fig. 1A). At the same time, the content of CS in CT conjugates was 81.01 ± 4.83% (w/w) which was measured by phloroglucinol color reaction.

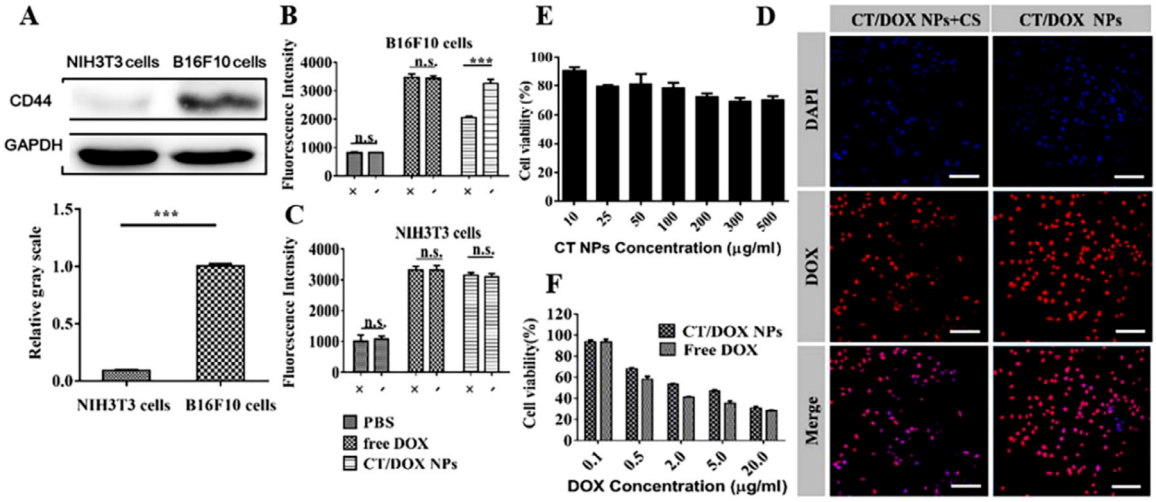

Fig. 2 – Cellular Experiments. (A) Western blot assay of the expression of CD44 receptor on B16F10 and NIH 3T3 cells. (B, C) Flow cytometer result of the competitive inhibition study on B16F10 and NIH3T3 cells after an incubation with free DOX and CT/DOX NPs (at equivalent dose of 2.5 μg/ml DOX, the concentration of free CS was 2 mg/ml) respectively for 2 h. (D) The CLSM images of B16F10 cells treated with CT/DOX NPs (at equivalent dose of 2.5 μg/ml DOX, the concentration of free CS was 2 mg/ml) respectively for 2 h. DAPI-stained cell nucleus channel (blue). DOX channel (red). Scale bar 50 μm. (E) Results of the cytotoxicity assay of CT NPs at different concentrations in B16F10cells (mean ± SD, $n = 5$). (H) Results of the cytotoxicity assay of free DOX and CT/DOX NPs at different concentrations in B16F10 cells (mean ± SD, $n = 5$).

3.2. *Critical micelle concentration (CMC) of the CT NPs*

CMC value indicates the stability of the micelles when subjects the dilution effect *in vivo*, and also represents the ability of the polymer to self-assemble in solution. With the increment of CT concentrations, pyrene gradually entered the nonpolar core of the micelle, meanwhile the I_1/I_2 value declined rapidly. Fig. 1B showed the fluorescence intensity ratio (I_1/I_2) of the logarithm of the CT NPs concentration. The data was fitted into two intersecting lines, and the CMC value of CT NPs was the concentration of intersection. The value was calculated to be 0.059 mg/ml, which indicated that CT NPs could form micelles at lower CT concentrations and withstand the blood dilution.

3.3. *DOX release from CT/DOX NPs*

CS and TOS were connected by ester bond, which could be degraded easily in the acid environment. We have investigated the release behavior of CT/DOX NPs in PBS buffer and plasma. In PBS buffer, as shown in Fig. 1C, after incubation with PBS (pH 7.4) for 48 h, only about 30% of the total DOX was released from CT/DOX NPs, while about 90% of DOX released in free DOX group. The results showed that CT/DOX NPs could remain stable under physiological conditions. In lysosomal environment (pH 5.0), almost 75% release was achieved, probably on account of the degradation of ester bond in CT conjugate.

In plasma, as shown in Fig. S8, due to the presence of esterase in plasma, the release of DOX from CT/DOX NPs in plasma was slightly increased than in PBS. However, after incubation with plasma for 12 h, the release of DOX from CT/DOX NPs was less than 40%, which is much lower than that of the free DOX group (about 90%). The result suggests that the esterase in the plasma may indeed cause the degradation of a small part of the ester bond and lead to the partial release of the drug. However, most of the CT NPs remain stable in the blood circulation, that may be due to the existence of steric hindrance, which affects the degradation of internal ester bonds by esterase.

3.4. *Hemolysis test and serum stability*

Hemolysis test was conducted to evaluated the blood compatibility of the CT NPs. As seen in Fig. 2C, the hemolysis of CT NPs at different concentrations was consistently lower than 5% within 8 h. At the same time, there was no aggregation of erythrocytes after exposing to CT NPs (Fig. 1F). All these results indicated that the CT NPs had minimum influence on the erythrocytes in blood. When the NPs were incubated with PBS or 50% FBS, the particle sizes (Fig. 1D) remained stable and the transmittance results (Fig. 1E) showed no obvious change within 24 h, suggesting that the NPs would be stable after intravenous injections.

3.5. *Cellular uptake and cytotoxicity assays of NPs*

As shown in Fig. 2A, the expression of CD44 receptors in B16F10 cells was relatively high, while the expression was quite low on NIH 3T3 cells. Therefore, NIH 3T3 cells were selected as a negative control. Subsequently, we conducted the competitive inhibition experiment to analyze the effects of CD44 receptors on cellular uptake. In the quantitative cellular uptake analysis (Fig. 2B and 2C), there was no

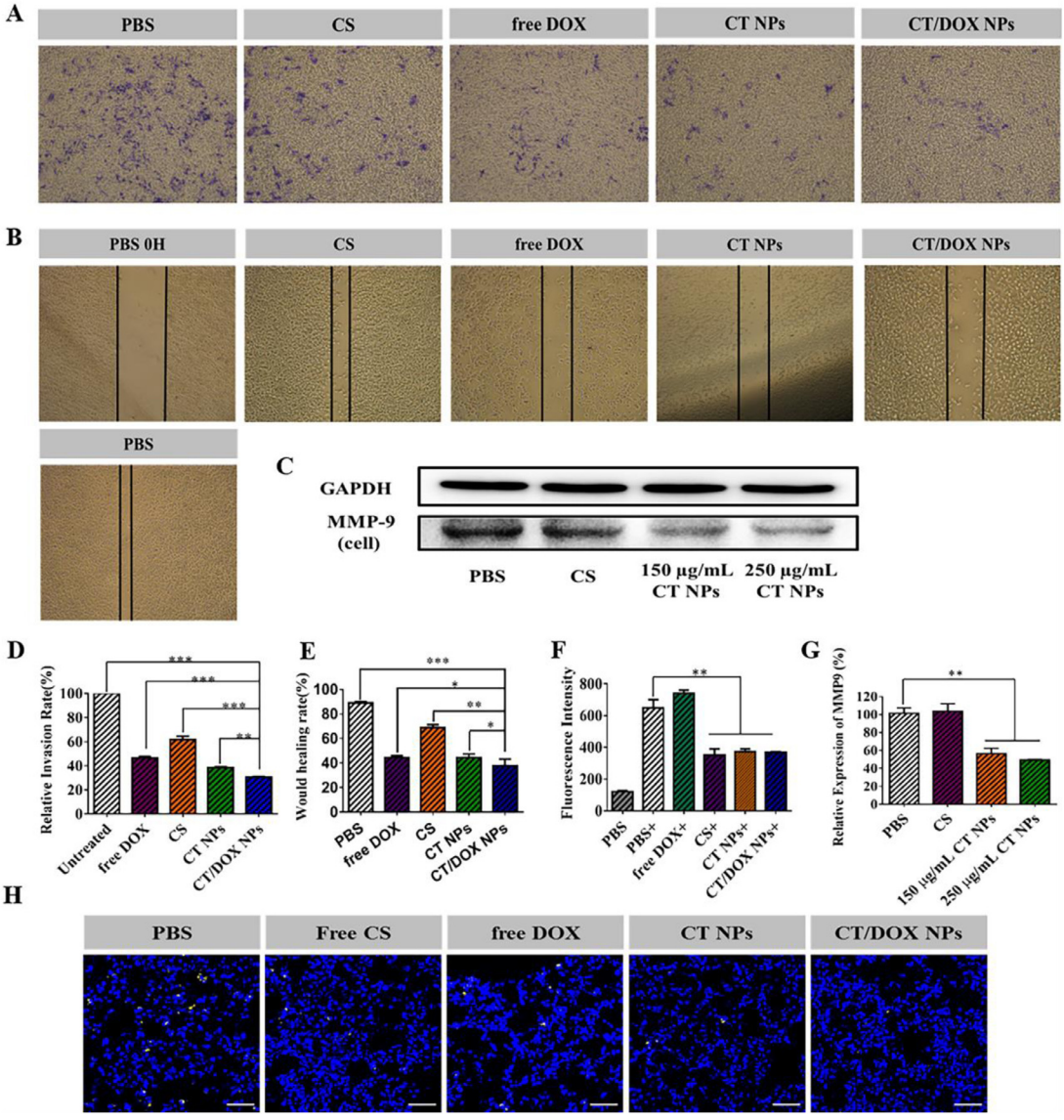

Fig. 3 – Inhibition effect of NPs on cell migration and invasion *in vitro* and anti-lung implantation. (A) Representative images and (D) quantitative analysis of invaded B16F10 cells after incubation with PBS, free CS, free DOX, CT NPs and CT/DOX NPs, respectively, for 48 h (mean ± SD, $n = 3$, ***P < 0.001, **P <0.01). (B) Representative Images and (E) quantitative analysis of scratch after incubation with PBS, free CS, free DOX, CT NPs or CT/DOX NPs, respectively, for 24 h (mean ± SD, $n = 3$, ***P < 0.001, **P < 0.01, *P < 0.05). (C) Western blot assay and (F) quantitative analysis of the expression of MMP-9 in B16F10 cells after treatment with different preparations for 30 h (mean ± SD, $n = 3$, **P < 0.01). (G) The fluorescence intensity of platelets adhering to B16F10 cells, "+" mean coincubation with calcein-AM-labeled platelets (mean ± SD, $n = 3$, **P < 0.01). (H) Representative CLSM images of the frozen sections of lungs, cell nuclei was stained by DAPI (blue), implanted B16F10 tumor cells were stained by CFSE (yellow). Scale bar: 50 μm.

significant difference in the free DOX groups when pre-incubated with free CS, while the uptake of the CT/DOX NPs groups was reduced in B16F10 cells. In comparison, the uptake efficiency of the CT/DOX NPs was almost the same in NIH 3T3 cells, regardless of the addition of free CS. CLSM images (Fig. 2D) in B16F10 cells exhibited similar results. Based on these results, it can be concluded that the cellular uptake behavior of CT/DOX NPs was mediated by CD44 receptors.

CT NPs was almost nontoxic to B16F10 cells (Fig. 2E), as the cell viability remained more than 70% when the concentration of NPs ranged from 10 μg/ml to 500 μg/ml, indicating a good safety. As shown in Fig. 3F, both DOX and CT/DOX NPs displayed concentration-dependent cytotoxicity. When the B16F10 cells were treated with free DOX and CT/DOX NPs at the same DOX concentration, free DOX exhibited stronger cytotoxicity than CT/DOX NPs, which was due to the fact that free DOX diffused into the cells quickly and could kill cells

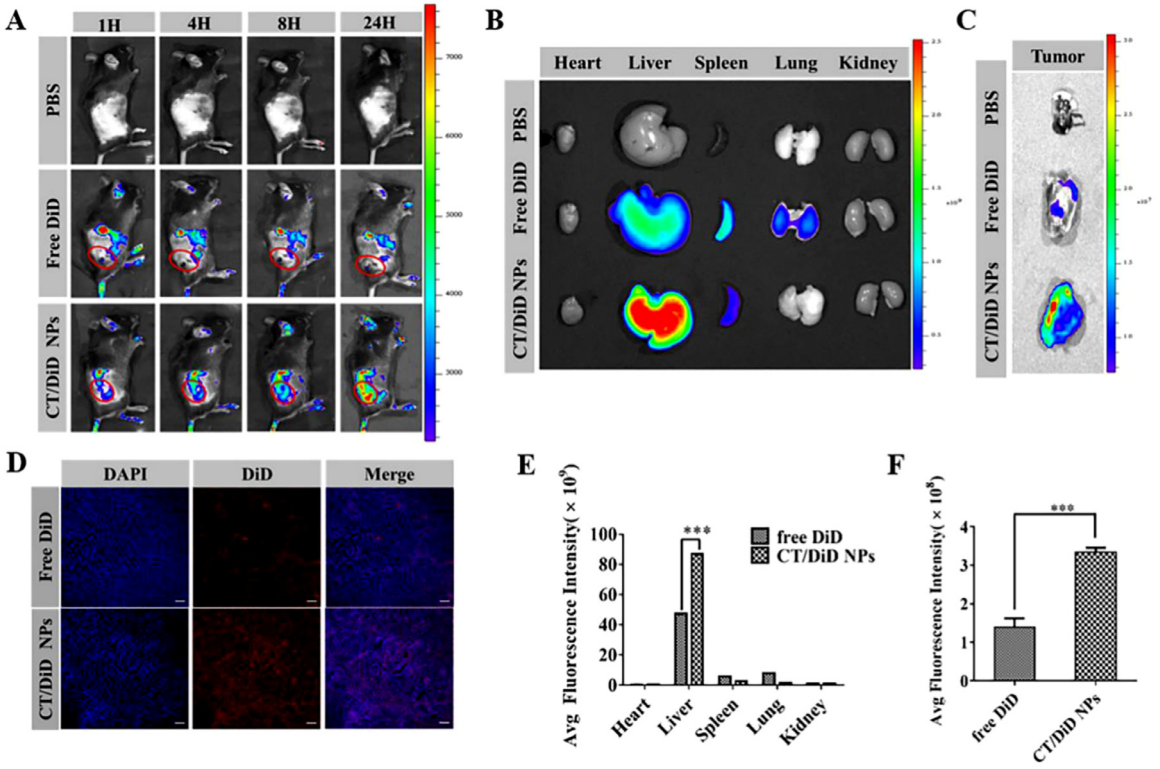

Fig. 4 – Bio-distribution of CT/DOX NPs *in vivo*. (A) Representative images of DiD in the tumor site of B16F10 tumor-bearing mice at 1, 4, 8 and 24 h. (B) Representative *ex vivo* images and E) semiquantitative mean fluorescence intensity of organs at 24 h after the systemic administration of DiD-loaded NPs. (mean ± SD, $n = 3$, ***$P < 0.001$). (C) Representative ex vivo images and F) semiquantitative mean fluorescence intensity of tumors at 24 h after the systemic administration of DiD-loaded NPs. (mean ± SD, $n = 3$, ***$P < 0.001$). (D) Representative CLSM images of tumor tissue frozen sections from B16F10 tumor-bearing mice 24 h after systemic administration of DiD-loaded NPs, showing DiD channel (red), and DAPI-stained nucleus channel (blue), Scale bar 200 mm.

directly at cellular level. The ability of CT/DOX NPs to induce apoptosis was inspected by Annexin V-FITC / PI apoptosis detection kit (Fig. 2F). Compared with CT/DOX NPs group, a higher apoptosis ratio was observed in free DOX group, which was consistent with the cytotoxicity test.

3.6. *In vitro inhibition of cell migration and invasion*

In the wound-healing assay (Fig. 3B and 3E), the relative wound healing rate of PBS group reached 88.97% ± 1.07% after 24 h and was slightly inhibited by CS and CT NPs. Surprisingly, the CT/DOX NPs obviously reduced the healing by 34.43% ± 2.83%, indicating that CT/DOX NPs had optimal inhibitory effects on cell migration.

In the invasion assays. Similar with the migration assay, cells in the PBS groups easily penetrated the Matrigel-coated membrane and crossed into the lower chamber. CS-treated group had a slightly inhibition on invasion and the relative invasion ratio was 61.70% ± 0.90%, whereas CT NPs-treated and CT/DOX NPs-treated groups showed strong inhibitory effects on invasion, reducing the relative invasion ratio to 38.40% ± 0.90% and 30.51% ± 0.74%, respectively (Fig. 3A and 3D). The results indicated that TOS played an essential role in cell invasion.

A variety of tumor cells, including B16F10 melanoma cells secrete MMP-9 to degrade the extracellular matrix. This phenomenon facilitates cell dissemination from the primary site, invasion and the ultimate entry into the blood vessels. Based on the previous research results of our group, TOS can reduce the secretion of MMP-9 in tumor cells [28,47]. Here, the secretion of MMP-9 in B16F10 cells was test by Western blot assay (Fig. 3C and 3F). The result confirmed that the secretion of MMP-9 could be markedly reduced when treated with 150 μg/ml blank NPs owing to the function of TOS. However, CS had no significant function on MMP-9 expression in tumor cells.

3.7. *The inhibitory effect of CT/DOX NPs on the adherence between platelets and tumor cells*

Human blood contains abundant circulating platelets, which can significantly assist tumor metastasis [6,10]. According to the fluorescence quantitative study Fig. 3G, the calcein-AM signal in CS group was markedly reduced, just as the CT NPs and CT/DOX NPs ($P < 0.01$), suggesting that CS could reduce the adherence of tumor cells to platelets. In addition, *in vivo* assay of the implantation of B16F10 cells in lung tissue was conducted. The images of frozen lung sections were shown in

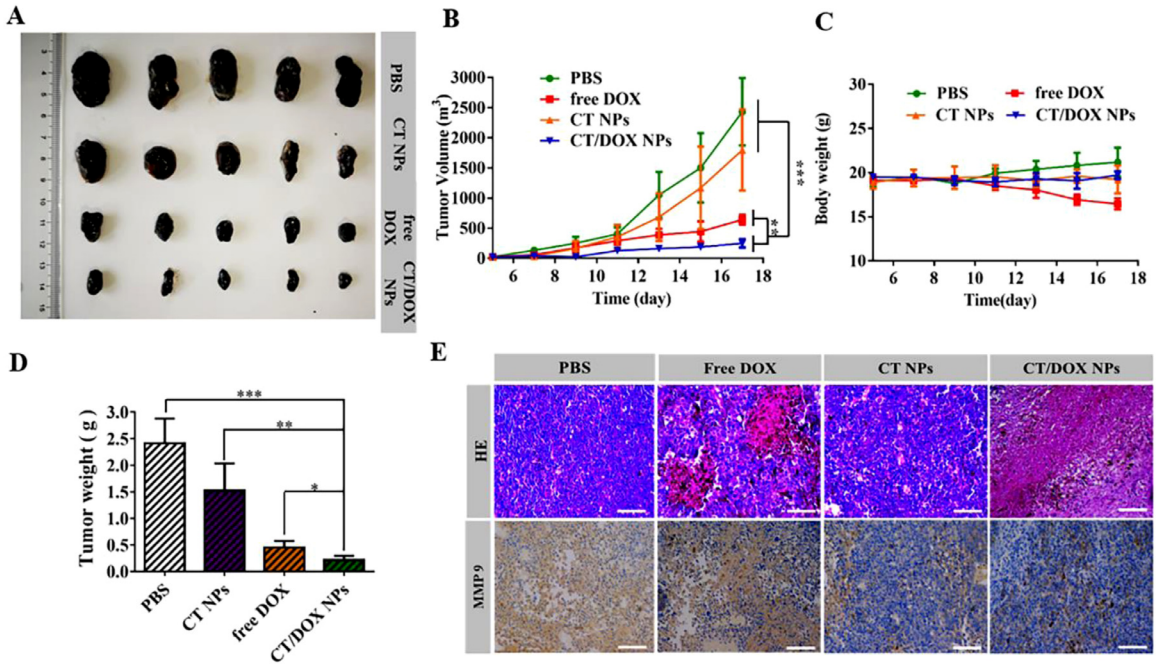

Fig. 5 – B16F10 subcutaneous tumor treatment. (A) Images of B16F10 tumors harvested from C57BL/6 mice after treating with PBS, CT NPs, free DOX, CT/DOX NPs (at an equivalent dose of DOX 3 mg/kg), respectively. (B) Tumor growth curves of various groups (mean ± SD, $n = 5$, $^{**}P < 0.01$ and $^{***}P < 0.001$). (C) Body weight curves of various groups (mean ± SD, $n = 5$). (D) Weights of the harvested B16F10 tumors (mean ± SD, $n = 5$, $^{*}P < 0.05$, $^{**}P < 0.01$ and $^{***}P < 0.001$). (E) Hematoxylin and eosin (H&E) staining and immunohistochemical staining of MMP-9 for B16F10 tumors. Scale bar: 100 μm.

Fig. 3H. Free CS, CT NPs and CT/DOX NPs all could lessen the adherence between platelets and tumor cells.

3.8. *In vivo tumor-targeting effect*

The accumulation of fluorescence at tumor sites was shown in the images (Fig. 4A). With the prolonging of time, the fluorescence intensity of CT/DiD NPs group was gradually increased, which was higher than free DiD group at any point of time. Meanwhile, in the images of organs (Fig. 4B and 4E), the signal of CT/DiD NPs was principally observed in liver, which may be owing to the reticuloendothelial system and CD44 receptors in the liver. At the same time, the fluorescence of CT/DiD NPs in tumor site was about two times as high as that of free DiD at 24 h (Fig. 4C and 4F). The images of frozen tumor sections (Fig. 4D) showed high fluorescence of CT NPs in central area at 24 h.

3.9. *In vivo anti-tumor efficacy*

The B16F10 subcutaneous tumor transplantation model was constructed to evaluate the *in vivo* antitumor effect of CT/DOX NPs. As shown in (Fig. 5A), the tumors isolated from PBS-treated and CT NPs-treated mice exhibited rapid tumor growth, while the tumor volume and the average tumor weight in CT/DOX NPs were the lowest (Fig. 5A and 5D). At the same time, no significant change was found in the body weight except for the free DOX group (Fig. 5C). The mean tumor growth inhibition ratio of CT NPs, free DOX and CT/DOX NPs groups were 26.14%, 73.54% and 89.69%, respectively, compared to the PBS control group. As shown in Fig. 5E, c staining analysis indicated that mice treated with PBS and CT NP maintained their complete microstructures. However CT/DOX NPs group exhibited the maximum areas of cell necrosis and apoptosis, suggesting that CT/DOX NPS had an enhanced inhibitory effect on tumor growth.

Moreover, immunohistochemical analysis indicated that CT NPs and CT/DOX NPs could interfere the expression of MMP-9 in tumor (Fig. 5E), which was consistent with the western blot results at the cellular level. Hence, TOS was able to reduce tumor cells from extravasating into blood vessels and exerting anti-metastases effect. Pathological observation of main organs further confirmed the superiority of CT/DOX NPs, the myocardial fiber in the free DOX group showed obvious fracture phenomenon, indicating that DOX had some damage to the heart. Whereas, the microstructure of the main organs was clear and complete in other groups, without any abnormal performance (Fig. S8I).

3.10. *In vivo anti-metastasis efficacy*

The lungs were harvested and imaged on Day 24, metastatic nodules were counted simultaneously. As shown in Fig. 6A, a large number of metastasis nodules were found in the PBS group indicated that B16F10 cells had a tendency to migrate to the lungs and. Due to its own toxic effect, free DOX could directly kill circulating tumor cells after being injected through tail vein. CS can interfere the adherence between tumor cells and platelets, therefore, the number of pulmonary metastasis nodules reduced in the CS group.

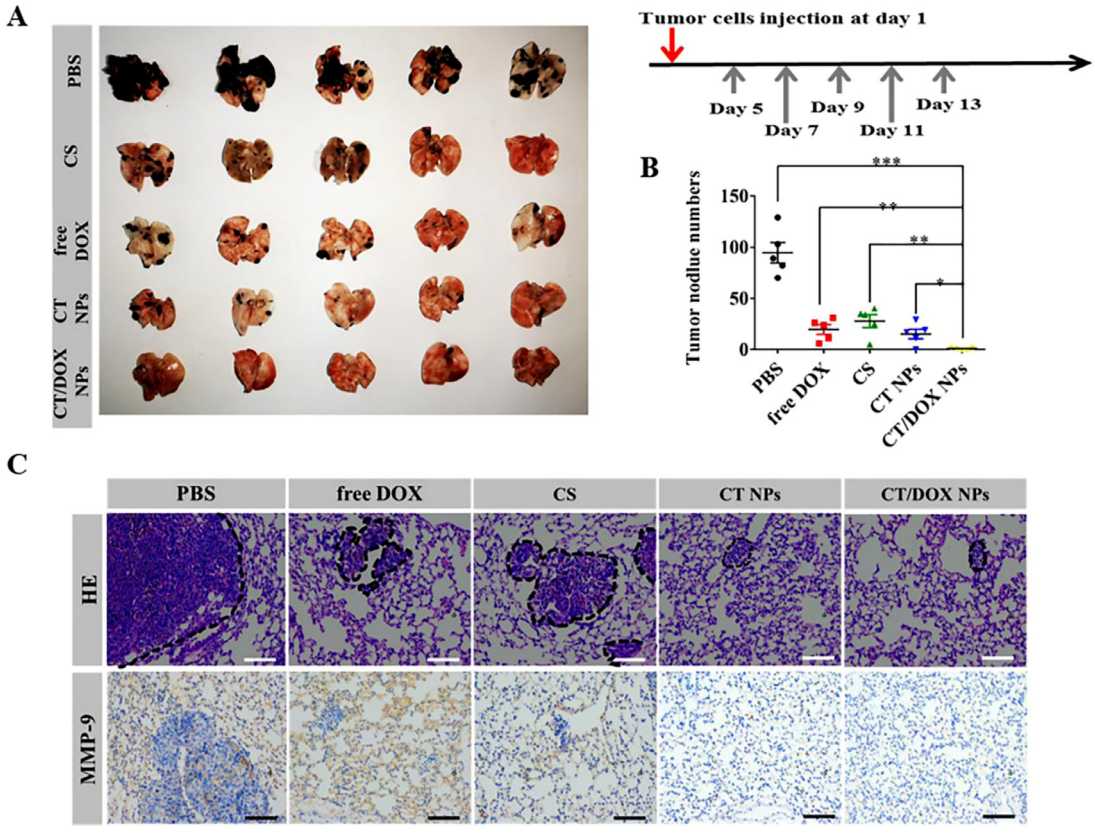

Fig. 6 – *In vivo* anti-metastasis treatment. (A) Images of lungs excised from C57BL/6 mice after treating with PBS, free DOX, free CS, CT NPs and CT/DOX NPs (at an equivalent dose of DOX 3 mg/kg), respectively. (B) Numbers of the pulmonary metastatic nodules (mean ± SD, $n = 5$, *$P < 0.05$, **$P < 0.01$ and ***$P < 0.001$. (C) H&E staining and immunohistochemical staining of MMP-9 for lungs. Scale bar: 100 μm.

TOS would reduce the secretion of MMP-9 in tumor cells; therefore, the number of metastasis nodules in the CT NPs group was further reduced compared with the CS group. As for mice treated with CT/DOX NPs, there were few visible metastasis nodules (Fig. 6B). This was owing to the CT NPs could not only prevent tumor cells adhering to platelets, but also interfere the secretion of MMP-9 in tumor cells, while DOX could kill tumor cells directly. Thereby, CT/DOX NPs effectively reduced B16F10 cells implant in organs. In Fig. 6C, 6H and 6E staining exhibited similar result, the lesion areas of the CT/DOX NPs group were the smallest compared with other groups, showing the best inhibitory effect on the lung metastasis of melanoma cells. In addition, it has been reported that premetastatic niche will remodel extracellular matrix (ECM) through the overexpression of MMP-9 to support the seeding and survival of circulating tumor cells [23,46,47]. Immunohistochemical staining of lungs (Fig. 6C) demonstrated that CT NPs and CT/DOX NPs would markedly lesson the expression level of MMP-9, which indicated an suppression effect on implantation in lung.

3.11. *Preliminary safety of CT/DOX NPs*

DOX as one of the most effective chemotherapy drugs, are widely used in various types of cancer. While free DOX has many side effects, for example, decreases of platelets and white blood cells, damages to heart and liver function. So, hematological analysis was conducted to estimate the preliminary safety. In Fig. S9A and Fig. S9C, free DOX-treated led to a downward trend in the number of WBC (white blood cells) and RBC (red blood cells) in healthy mice. These results suggested that free DOX could affect bone marrow hematopoietic function. In comparison, CT/DOX NPs-treated group did not exhibit obvious decrease in the counts of WBC and RBC, indicating CT/DOX NPs could reduce the toxicity of free DOX. In addition, the toxicity of formulations to organ was conducted through a biochemical analysis (Fig.S9D, S9E and S9F). Free DOX markedly augment the levels of AST (aspartate transaminase), ALT (alanine aminotransferase) and CK (creatine kinase), suggesting that free DOX might cause liver and heart injury. But CT/DOX NPs would lessen the injuries of liver and heart. The preliminary safety evaluation verified that CT/DOX NPs was biocompatible and safe for injection.

4. Conclusion

Here, we have established a self-delivering micellar system CT that worked as both antimetastatic agent and nanocarrier. The hydrophobic segment TOS and the hydrophilic segment CS are biocompatible materials, meanwhile, CT NPs delivered

the chemotherapy drug DOX to tumor site without causing severe toxicity, which presented a potent treatment for solid tumor and metastasis. At cellular level, the uptake of NPs was mediated by CS and CD44 receptors; in addition, CT/DOX NPs exhibited excellent inhibitory effect on cell migration and invasion. Owing to the EPR effect and interaction between CS and CD44 receptors, CT/DOX NPs could accumulate effectively in tumor site *in vivo*. Besides, CT/DOX NPs had the best inhibitory effect on tumor growth. More importantly, it could also prevent the tumor cells from implanting in lung. Notably, the inhibition of CT/DOX NPs on tumor metastasis was attributed to the nanocarrier itself which could affect different phases of the metastatic cascade. We have proven that CT NPs would decrease the secretion of MMP-9 in B16F10 cells, reducing the shedding of tumor cells from the primary site and eventually preventing it entering the circulation. CT NPs could also interfere the adherence between tumor cells and platelets, which would lead to a reduction of tumor cells on implanting at metastatic organs. In summary, the multifunctional CT/DOX NPs was a promising therapeutic nanosystem for the treatment of both primary and metastatic cancer.

Conflicts of interest

The authors declare no conflicts of interest

Acknowledgments

This work was supported by Major Projects of the National Natural Science Foundation of China (81974499), Sichuan Science and Technology Program (2018RZ0136) and Sichuan Veterinary Medicine and Drug innovation Group of China Agricultural Research System (SCCXTD-2020-18).

Supplementary materials

Supplementary material associated with this article can be found, in the online version, at doi:10.1016/j.ajps.2021.08.002.

REFERENCES

[1] Mohme M, Riethdorf S, Pantel K. Circulating and disseminated tumour cells - mechanisms of immune surveillance and escape. Nat Rev Clin Oncol 2017;14(3):155–67.
[2] Chaffer CL, Weinberg RA. A perspective on cancer cell metastasis. Science 2011;331(6024):1559–64.
[3] Steeg PS. Tumor metastasis: mechanistic insights and clinical challenges. Nat Med 2006;12(8):895–904.
[4] Weigelt B, Peterse JL, van 't Veer LJ. Breast cancer metastasis: markers and models. Nat Rev Cancer 2005;5(8):591–602.
[5] Fidler IJ. The pathogenesis of cancer metastasis: the 'seed and soil' hypothesis revisited. Nat Rev Cancer 2003;3(6):453–8.
[6] Zhang Y, Wei J, Liu S, Wang J, Han X, Qin H, et al. Inhibition of platelet function using liposomal nanoparticles blocks tumor metastasis. Theranostics 2017;7(5):1062–71.
[7] Peer D, Karp JM, Hong S, Farokhzad OC, Margalit R, Langer R. Nanocarriers as an emerging platform for cancer therapy. Nat Nanotechnol 2007;2(12):751–60.
[8] Valastyan S, Weinberg RA. Tumor metastasis: molecular insights and evolving paradigms. Cell 2011; 147(2):275–92.
[9] Joyce JA, Pollard JW. Microenvironmental regulation of metastasis. Nat Rev Cancer 2009;9(4):239–52.
[10] Eckhardt BL, Francis PA, Parker BS, Anderson RL. Strategies for the discovery and development of therapies for metastatic breast cancer. Nat Rev Drug Discov 2012;11(6):479–97.
[11] Sethi N, Kang Y. Unravelling the complexity of metastasis - molecular understanding and targeted therapies. Nat Rev Cancer 2011;11(10):735–48.
[12] Lv Y, Xu C, Zhao X, Lin C, Yang X, Xin X, et al. Nanoplatform assembled from a CD44-targeted prodrug and smart liposomes for dual targeting of tumor microenvironment and cancer cells. ACS Nano 2018;12(2):1519–36.
[13] Sparano JA, Bernardo P, Stephenson P, Gradishar WJ, Ingle JN, Zucker S, et al. Randomized phase III trial of marimastat *versus* placebo in patients with metastatic breast cancer who have responding or stable disease after first-line chemotherapy: eastern Cooperative Oncology Group trial E2196. J Clin Oncol 2004;22(23):4683–90.
[14] Ye H, Wang K, Wang M, Liu R, Song H, Li N, et al. Bioinspired nanoplatelets for chemo-photothermal therapy of breast cancer metastasis inhibition. Biomaterials 2019;206:1–12.
[15] Lee A, Djamgoz MBA. Triple negative breast cancer: emerging therapeutic modalities and novel combination therapies. Cancer Treat Rev 2018;62:110–22.
[16] Carmeliet P, Jain RK. Molecular mechanisms and clinical applications of angiogenesis. Nature 2011;473(7347):298–307.
[17] Clause KC, Barker TH. Extracellular matrix signaling in morphogenesis and repair. Curr Opin Biotechnol 2013;24(5):830–3.
[18] Theocharis AD, Skandalis SS, Gialeli C, Karamanos NK. Extracellular matrix structure. Adv Drug Deliv Rev 2016;97:4–27.
[19] Frantz C, Stewart KM, Weaver VM. The extracellular matrix at a glance. J Cell Sci 2010;123(Pt 24):4195–200.
[20] Bernhard EJ, Gruber SB, Muschel RJ. Direct evidence linking expression of matrix metalloproteinase 9 (92-kDa gelatinase/collagenase) to the metastatic phenotype in transformed rat embryo cells. Proc Natl Acad Sci USA 1994;91(10):4293–7.
[21] Kessenbrock K, Plaks V, Werb Z. Matrix metalloproteinases: regulators of the tumor microenvironment. Cell 2010;141:52–67.
[22] Cottam D, Rees R. Regulation of matrix metalloproteinases - their role in tumor invasion and metastasis. Int J Oncol 1993;2(6):861–72.
[23] Hiratsuka S, Nakamura K, Iwai S, Murakami M, Itoh T, Kijima H, et al. MMP9 induction by vascular endothelial growth factor receptor-1 is involved in lung-specific metastasis. Cancer Cell 2002;2(4):289–300.
[24] Yu Q, Stamenkovic I. Localization of matrix metalloproteinase 9 to the cell surface provides a mechanism for CD44-mediated tumor invasion. Genes Dev 1999;13(1):35–48.
[25] Angulo-Molina A, Reyes-Leyva J, Lopez-Malo A, Hernandez J. The role of alpha tocopheryl succinate (alpha-TOS) as a potential anticancer agent. Nutr Cancer 2014;66(2):167–76.
[26] Malafa MP, Fokum FD, Mowlavi A, Abusief M, King M. Vitamin E inhibits melanoma growth in mice. Surgery 2002;131(1):85–91.

[27] Duhem N, Danhier F, Preat V. Vitamin E-based nanomedicines for anti-cancer drug delivery. J Control Release 2014;182:33–44.
[28] Long Y, Lu Z, Xu S, Li M, Wang X, Zhang Z, et al. Self-delivery micellar nanoparticles prevent premetastatic niche formation by interfering with the early recruitment and vascular destruction of granulocytic myeloid-derived suppressor cells. Nano Lett 2020;20(4):2219–29.
[29] Labelle M, Begum S, Hynes RO. Platelets guide the formation of early metastatic niches. Proc Natl Acad Sci USA 2014;111(30):E3053–61.
[30] Gay LJ, Felding-Habermann B. Contribution of platelets to tumour metastasis. Nat Rev Cancer 2011;11(2):123–34.
[31] Karpatkin S, Pearlstein E, Ambrogio C, Coller BS. Role of adhesive proteins in platelet tumor interaction *in vitro* and metastasis formation *in vivo*. J Clin Invest 1988;81(4):1012–19.
[32] Stanger BZ, Kahn ML. Platelets and tumor cells: a new form of border control. Cancer Cell 2013;24(1):9–11.
[33] Labelle M, Begum S, Hynes RO. Direct signaling between platelets and cancer cells induces an epithelial-mesenchymal-like transition and promotes metastasis. Cancer Cell 2011;20(5):576–90.
[34] Rao W, Wang H, Han J, Zhao S, Dumbleton J, Agarwal P, et al. Chitosan-decorated doxorubicin-encapsulated nanoparticle targets and eliminates tumor reinitiating cancer stem-like cells. ACS Nano 2015;9(6):5725–40.
[35] Cho JH, Lee SC, Ha NR, Lee SJ, Yoon MY. A novel peptide-based recognition probe for the sensitive detection of CD44 on breast cancer stem cells. Mol Cell Probes 2015;29(6):492–9.
[36] Fujimoto T, Kawashima H, Tanaka T, Hirose M, Toyama-Sorimachi N, Matsuzawa Y, et al. CD44 binds a chondroitin sulfate proteoglycan, aggrecan. Int Immunol 2001;13(3):359–66.
[37] Beldman TJ, Senders ML, Alaarg A, Perez-Medina C, Tang J, Zhao Y, et al. Hyaluronan nanoparticles selectively target plaque-associated macrophages and improve plaque stability in atherosclerosis. ACS Nano 2017;11(6):5785–99.
[38] Luo J, Zhang P, Zhao T, Jia M, Yin P, Li W, et al. Golgi apparatus-targeted chondroitin-modified nanomicelles suppress hepatic stellate cell activation for the management of liver fibrosis. ACS Nano 2019;13(4):3910–23.
[39] Lim JJ, Temenoff JS. The effect of desulfation of chondroitin sulfate on interactions with positively charged growth factors and upregulation of cartilaginous markers in encapsulated MSCs. Biomaterials 2013;34(21):5007–18.
[40] Kim YJ, Borsig L, Varki NM, Varki A. P-selectin deficiency attenuates tumor growth and metastasis. Proc Natl Acad Sci USA 1998;95(16):9325–30.
[41] McEver RP. Selectin-carbohydrate interactions during inflammation and metastasis. Glycoconj J 1997;14(5):585–91.
[42] Cooney CA, Jousheghany F, Yao-Borengasser A, Phanavanh B, Gomes T, Kieber-Emmons AM, et al. Chondroitin sulfates play a major role in breast cancer metastasis: a role for CSPG4 and CHST11 gene expression in forming surface P-selectin ligands in aggressive breast cancer cells. Breast Cancer Res 2011;13(3):R58.
[43] Monzavi-Karbassi B, Stanley JS, Hennings L, Jousheghany F, Artaud C, Shaaf S, et al. Chondroitin sulfate glycosaminoglycans as major P-selectin ligands on metastatic breast cancer cell lines. Int J Cancer 2007;120(6):1179–91.
[44] Schroeder A, Heller DA, Winslow MM, Dahlman JE, Pratt GW, Langer R, et al. Treating metastatic cancer with nanotechnology. Nat Rev Cancer 2011;12(1):39–50.
[45] Mei L, Liu Y, Xia C, Zhou Y, Zhang Z, He Q. Polymer-drug nanoparticles combine doxorubicin carrier and heparin bioactivity functionalities for primary and metastatic cancer treatment. Mol Pharm 2017;14(2):513–22.
[46] Gao H, Liu K, Yu ZD, Geng FS. Spectrophotometric determination of chondroitin sulfate with phlor glucinol. Chin J Biochem Pharm 2000(05):33–4.
[47] Guo R, Long Y, Lu Z, Deng M, He P, Li M, He Q. Enhanced stability and efficacy of GEM-TOS prodrug by co-assembly with antimetastatic shell LMWH-TOS. Acta Pharm Sin B 2019;10(10):1977–88.